Draft version May 20, 2026
Typeset using LaTeX default style in AASTeX631

Gaia21bja: pre-main sequence star with quasi-periodic bursts

Ádám Mátéfy,[1] Zsófia Nagy,[2,3] Ágnes Kóspál,[2,3,4] Péter Ábrahám,[2,3,4,5] Fernando Cruz-Sáenz de Miera,[6,2,3] Máté Szilágyi,[2,3] Michał Siwak,[7,2,3] Eleonora Fiorellino,[8,9] Teresa Giannini,[10] Mária Kun,[2,3] László Szabados,[2,3] Gábor Marton,[2,3] Patrik Németh,[4,2,3] Brunella Nisini,[10] and Zsófia Marianna Szabó[11,12,2,3]

[1]*Nagoya University, School of Science, Department of Physics, G30 Physics Program, 1 Furo-cho, Chikusa-ku, Nagoya, Aichi, 464-8602, Japan*

[2]*Konkoly Observatory, HUN-REN Research Centre for Astronomy and Earth Sciences Konkoly-Thege Miklós út 15-17, H-1121 Budapest, Hungary*

[3]*CSFK, MTA Centre of Excellence, Konkoly-Thege Miklós út 15-17, 1121 Budapest, Hungary*

[4]*ELTE Eötvös Loránd University, Institute of Physics and Astronomy, Pázmány Péter sétány 1A, Budapest 1117, Hungary*

[5]*Department of Astrophysics, University of Vienna, Türkenschanzstr. 17, 1180, Vienna, Austria*

[6]*Institut de Recherche en Astrophysique et Planétologie, Université de Toulouse, UT3-PS, OMP, CNRS, 9 av. du Colonel Roche, 31028 Toulouse Cedex 4, France*

[7]*Mt. Suhora Astronomical Observatory, University of the National Education Commission, ul. Podchorażych 2, 30-084 Kraków, Poland*

[8]*Alma Mater Studiorum – Università di Bologna, Dipartimento di Fisica e Astronomia "Augusto Righi", Via Gobetti 93/2, I-40129, Bologna, Italy*

[9]*INAF - Osservatorio Astronomico di Trieste, via Tiepolo 11, I-34143 Trieste, Italy*

[10]*INAF-Osservatorio Astronomico di Roma, via di Frascati 33, 00078, Monte Porzio Catone, Italy*

[11]*Max Planck Institute for Radio Astronomy, Auf dem Hügel 69, 53121 Bonn, Germany*

[12]*Scottish Universities Physics Alliance (SUPA), School of Physics and Astronomy, University of St Andrews, North Haugh, St Andrews, KY16 9SS, UK*

ABSTRACT

Gaia21bja is a Gaia alerted young stellar object (YSO) that exhibits at least seven quasi-peridoic brightenings over a 20 year-long light curve with durations of 1.5-2 years and amplitudes up to ∼1.7 mag in the Gaia G-band. We analyze its optical and near-infrared photometry and spectra taken using the IRTF and VLT in its faint and bright states in order to characterize its physical properties. A Lomb-Scargle periodogram analysis results in a most significant period of 916 ± 77 days. We derived the stellar parameters as $R_\star = 0.78 \pm 0.04\ R_\odot$, $L_\star = (4.5 \pm 0.3) \times 10^{-2}\ L_\odot$, and $M_\star = 0.16 \pm 0.03\ M_\odot$. The spectra taken during the burst are dominated by emission lines and are similar to those of EX Lupi-type eruptive young stars (EXors). We found that the accretion luminosity and mass accretion rate increased by a factor of $5.5 - 6$ during the burst. Based on this, and the quasi-periodic bursts, we suggest that Gaia21bja is an eruptive YSO, and is most consistent with the 'Periodic' category of the Outbursting YSOs Catalogue.

Keywords: Eruptive variable stars(476) – Stellar accretion(1578) – Pre-main sequence stars(1290) – Star formation(1569)

1. INTRODUCTION

Young stellar objects (YSOs) show variability due to various physical processes, such as accretion and circumstellar extinction (Fischer et al. 2023). The most important process is the former, which can produce variability with a wide range of time scales and amplitudes. Most YSOs show variability with typical time scales from hours to days and

matefy.adam.s7@s.mail.nagoya-u.ac.jp

nagy.zsofia@csfk.org

with amplitudes below 1 mag. Longer episodes with increased accretion rates also occur and were proposed to explain the observed luminosities of YSOs, which were found to be lower than the expectations (Kenyon et al. 1990). Such events include bursts and outbursts as recently defined by Fischer et al. (2023). Bursts typically occur on time scales from months to a year with amplitudes of 1–2.5 mag. Outbursts produce even larger amplitudes, ∼2.5–6 mag on time scales from months to years to even a century.

Young stellar objects that experience episodic accretion are called eruptive young stars, and are traditionally classified into two main groups: EX Lupi-type stars (EXors, Herbig 2008) and FU Orionis-type stars (FUors, Herbig 1977). EXors produce bursts or outbursts that last between a month up to a year, some of which are repeated non-periodically every few years, while FUors are in outburst for multiple years or decades. In addition to their time scale, EXors produce bursts/outbursts with typical mass accretion rates of a few 10^{-7} $M_{\odot}$ yr^{-1} (Contreras Peña et al. 2025 and references therein), while FUor outbursts can have mass accretion rates in excess of 10^{-4} $M_{\odot}$ yr^{-1} (Fischer et al. 2023 and references therein). Their spectra also show key differences: EXors display rich emission-line spectra, similar to classical T Tauri type stars (CTTS), whereas FUor spectra are dominated by absorption lines. The optical spectra of EXors are dominated by emission lines thought to be produced in magnetospheres and accretion shocks while the optical-near IR spectra of FUors are dominated by absorption lines produced in the accretion disk (Audard et al. 2014, Fischer et al. 2023, Liu et al. 2022).

A decade ago, only about 40 eruptive young stars were known (Audard et al. 2014). Currently there are 173 confirmed eruptive YSOs and 355 candidates, according to the new catalog of outbursting YSOs (OYCAT, Contreras Peña et al. 2025)[1]. This increase is due to transient surveys including the Gaia Photometric Science Alerts (Hodgkin et al. 2021) with its 4π sky coverage and approximately monthly cadence. Several discoveries of eruptive young stars have been made using the Gaia Alerts in recent years, such as four FUors: Gaia17bpi (Hillenbrand et al. 2018), Gaia18dvy (Szegedi-Elek et al. 2020), Gaia21elv (Nagy et al. 2023), and Gaia20bdk (Siwak et al. 2025). Other objects, such as Gaia20eae (Cruz-Sáenz de Miera et al. 2022; Ghosh et al. 2022), Gaia19fct (Park et al. 2022), and Gaia23bab (Giannini et al. 2024; Nagy et al. 2025), Gaia21bkw (Giannini et al. 2026), and Gaia24beh (Giannini et al. 2026) were identified as EXors. Some Gaia alerted eruptive YSOs showed both FUor and EXor properties, such as Gaia19ajj (Hillenbrand et al. 2019), Gaia19bey (Hodapp et al. 2020), Gaia21bty (Siwak et al. 2023), Gaia18cjb (Fiorellino et al. 2024), and Gaia20dsk (Németh et al. 2026). Another young star, Gaia20fgx, showed brightness variations similar to EXors, however, its mass accretion rate was found to be closer to those of CTTS rather than the values measured for eruptive YSOs (Nagy et al. 2022). Giannini et al. (2026) found, based on a sample of 16 Gaia alerted YSOs, that those which exhibit variability with amplitudes of $\Delta G \gtrsim 2$ mag and $W1 \gtrsim 1$ mag are likely EXors.

However, episodic accretion can manifest in smaller scale bursts too, such as the 'bursters' reported by Findeisen et al. (2013), Cody & Hillenbrand (2018), and Lakeland & Naylor (2022). Bursters occur on shorter time scales compared to eruptive YSOs, i.e., from days-months and with typical amplitudes of 1-2 mag in the R-band (Findeisen et al. 2013). The mass accretion rate and its variability pattern is also expected to change with the evolutionary state of the YSO. For instance, variability amplitudes were shown to be larger for more embedded sources (Fischer et al. 2023 and references therein).

Gaia21bja (2MASS J16041416-2129151, WISE J160414.16-212915.5, Gaia DR3 6243394091902073728) had a Gaia alert on 2021 February 11 due to a brightening by about 1.5 mag. It is also included in the alerts of the Zwicky Transient Facility (ZTF, Patterson et al. 2018) as ZTF19aauxhac. It is located at $\alpha_{J2000} = 16^h04^m14.17^s$, $\delta_{J2000} = -21°29'15.28''$ at a distance of $d = 146.5 \pm 1.3$ pc (Bailer-Jones et al. 2021). Esplin et al. (2018) found that it has a disk that is optically thick at infrared wavelengths and has not yet significantly cleared primordial dust and gas, indicating that Gaia21bja is a YSO. Luhman et al. (2018) determined its spectral type as M4, corresponding to an effective temperature of 3190 ± 75 K (Thanathibodee et al. 2022). Luhman & Esplin (2020) estimated that its K band extinction is $A_K = 0.051$ mag, based on the $J - H$ color excess, and have also confirmed it to be a member of the Upper Scorpius star-forming region (Upper Sco). Ratzenböck et al. (2023a,b) also confirmed Gaia21bja to belong to Upper Sco.

In this paper, we analyze the physical properties of Gaia21bja and investigate whether it can be classified as an eruptive YSO. In Section 2 we summarize the available photometric and spectroscopic observations. In Section 3 we determine the stellar and accretion parameters of the star. We discuss our results in Section 4.

[1] http://starformation.synology.me:5002/OYCAT/main.html

2. OBSERVATIONS AND ARCHIVAL DATA

2.1. *Photometry*

We downloaded G band photometry from the *Gaia* Science Alerts Index website. We also downloaded the o ("orange", 560–820 nm) and c ("cyan", 420–650 nm) band magnitudes from the Asteroid Terrestrial-impact Last Alert System (ATLAS, Tonry et al. 2018, Smith et al. 2020, Heinze et al. 2018) survey using the ATLAS Forced Photometry web service (Shingles et al. 2021).

We used mid-infrared photometry from the Wide-field Infrared Survey Explorer (*WISE*, Wright et al. 2010, Wright et al. 2019) and *NEOWISE* (Mainzer et al. 2011, NEOWISE Team 2020) surveys from the NASA/IPAC Infrared Science Archive. *NEOWISE* observed the full sky on average twice a year with multiple exposures per epoch. For a comparison with the photometry from other instruments, we computed the average of multiple exposures of a single epoch. *NEOWISE* $W1$ and $W2$ photometry is known to display a photometric bias for saturated sources. We corrected for this bias using the correction curves given in the Explanatory Supplement to the *NEOWISE* Data Release Products (Cutri et al. 2015). We derived the average of the uncertainties of the single exposures (err1). We also calculated the standard deviation of the points we averaged per season (err2). For the error of the data points averaged per epoch we used the maximum of err1 and err2.

We also used photometry from the Catalina Real-Time Transient Survey (CRTS, Drake et al. 2009). We obtained V-band photometry from the Catalina Surveys Data Release DR2[2]. The CRTS covered ∼33,000 square degrees and provided light curves for about 500 million objects with V magnitudes between 11.5 mag and 21.5 mag.

In addition to the archival photometry, we took JHK_s images of Gaia21bja with the infrared guiding camera of SpeX, a medium-resolution infrared spectrograph (Rayner et al. 2003) on the NASA Infrared Telescope Facility (IRTF) on Mauna Kea, Hawai'i (USA) on 22 July 2023 (Program ID: 2023A968; PI: Cruz Sáenz de Miera), on 10 August 2024 (Program ID: 2024B025, PI: Siwak), and on 2 March 2025 (Program ID: 2025A019, PI: Kóspál) using a 5-point dither pattern and 5 s exposures. We used the dithering to make a sky image which we subtracted from the shifted and co-added images. Finally we obtained aperture photometry for Gaia21bja and several other stars in the approximately $1' \times 1'$ field of view as comparison stars. We used the Two Micron All Sky Survey (2MASS, Skrutskie et al. 2003) for the photometric calibration. The resulting magnitudes are $J = 11.692 \pm 0.020$ mag, $H = 10.767 \pm 0.018$ mag, $K_s = 10.065 \pm 0.018$ mag on 22 July 2023, $J = 11.977 \pm 0.079$ mag, $H = 11.360 \pm 0.016$ mag, $K_s = 10.909 \pm 0.069$ mag on 10 August 2024, and $J = 12.022 \pm 0.058$ mag, $H = 11.355 \pm 0.023$ mag, $K_s = 10.911 \pm 0.068$ mag on 2 March 2025.

2.2. *Spectroscopy*

We obtained optical-infrared medium resolution spectra of Gaia21bja using the SpeX spectrograph (Rayner et al. 2003) at the 3.2 m diameter NASA Infrared Telescope Facility (IRTF) located on Mauna Kea, Hawai'i (USA) on 22 July 2023, 10 August 2024, and 2 March 2025. In all cases, we used the SXD grating covering the $0.7 - 2.55\,\mu$m range and the $0\farcs8$ wide slit, providing a spectral resolution of about 750. On 2 March 2025, we additionally used the LXD_long grating that covers $1.98 - 5.3\,\mu$m range and the $0\farcs8$ wide slit, providing a spectral resolution of about 940. Total exposure times ranged between 1079 s and 2158 s with the SXD grating and 389 s with the LXD_long grating. As telluric standards, we observed the A0 stars HD 133466 (on 22 July 2023) and HD 145127 (on 10 August 2024 and 2 March 2025) using the same instrumental setup as for the science target. We reduced all spectra in the same way using SpexTool (Vacca et al. 2003; Cushing et al. 2004). Data reduction steps included flat correction, subtraction of A and B nod positions, calculation of the spectroscopic traces on the 2D images, extraction of the 1D spectra in tapered apertures, division by the telluric spectra to correct for instrumental response and telluric absorption and emission, and the stitching of the various échelle orders. The telluric spectra were also used for a first estimate of the absolute flux calibration. We also derived synthetic photometry by multiplying the flux-calibrated spectra with the respective filter profiles, summing up the obtained values, and converting them from Jy to magnitude. We then scaled the spectra so that the synthetic photometry matches the photometry obtained with the guide camera. The scaling factor was 0.82 on 22 July 2023, 1.02 on 10 August 2024, and 1.02 on 2 March 2025, indicating that flux calibration with the telluric standard and the photometric comparison star give consistent results within 20% or better.

We obtained another spectrum on 9 February 2024 using the X-shooter instrument (Vernet et al. 2011), an echelle spectrograph mounted on the ESO Very Large Telescope (VLT) at the Paranal Observatory in Chile (Program ID:

[2] http://nesssi.cacr.caltech.edu/DataRelease

112.25XA; PI: Cruz-Sáenz de Miera). Covering the spectral range from 300 to 2500 nm, this instrument can simultaneously observe the ultraviolet (UVB), visible (VIS), and near-infrared (NIR) spectra. We used the $0.5'' \times 11''$, $0.4'' \times 11''$, and $0.4'' \times 11''$ size slits providing spectral resolutions of 9700, 18400, and 11600 in the UVB, VIS, and NIR arms, respectively. The exposure time for UVB, VIS, and NIR regions were 1492 s, 1536 s, 1600 s, respectively. We also measured Gaia21bja using the $5'' \times 11''$ slit to correct for slit losses and estimate the actual flux level by scaling the narrow slit spectrum to match the broad slit spectrum. The data were reduced using the X-shooter pipeline (Modigliani et al. 2010), and corrected for tellurics using MOLECFIT (Smette et al. 2015; Kausch et al. 2015). We calculated synthetic photometry based on the X-shooter spectrum, which resulted in $J = 11.604$ mag, $H = 10.931$ mag, and $K = 10.422$ mag.

3. RESULTS

3.1. *Light and color variations*

Figure 1 shows the long-term light curve of Gaia21bja, covering about 20 years, showing at least seven brightenings with amplitudes up to ∼1.7 mag in the optical and durations of 1.5-2 years. By visual inspection, the brightenings may have a quasi-periodic behavior. In order to test this, we performed a Lomb-Scargle periodogram analysis based on the CRTS and Gaia G photometry obtained after 2011, using the public tools at the NASA Exoplanet Archive Periodogram Service[3]. The result is shown in Fig. 2. The most significant period was found to be $T = 916 \pm 77$ days, where we derived the error of the period by fitting a Gaussian to the peak of the periodogram. We used the half of the full width at half maximum (FWHM) value of the fitted Gaussian as the uncertainty of the period.

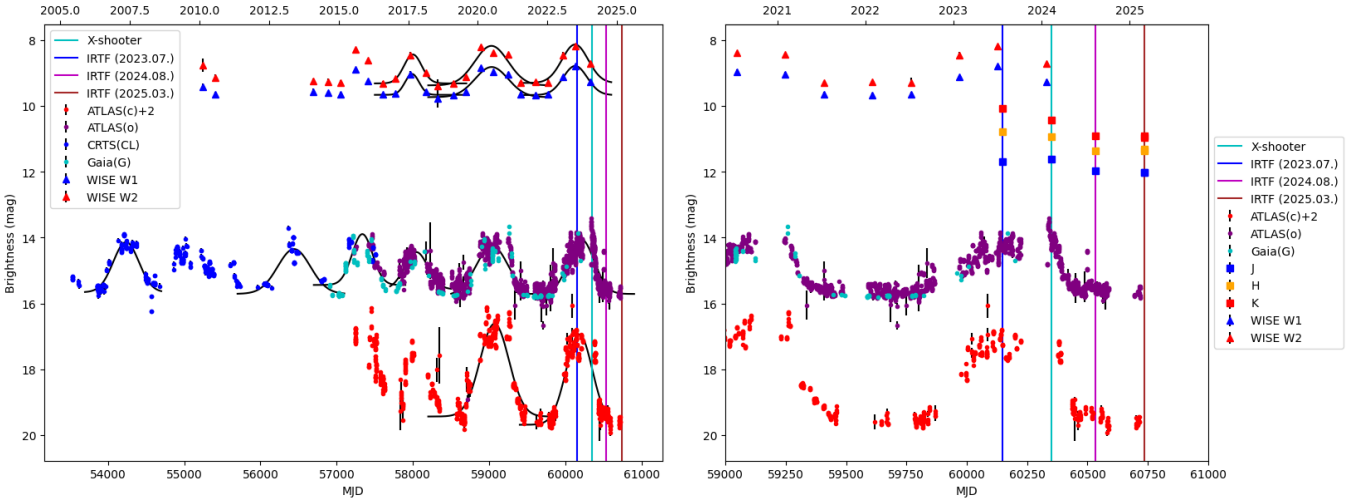

Figure 1. *Left panel:* Optical light curve of Gaia21bja based on ATLAS, Gaia G, and CRTS data covering about 20 years. *Right panel:* Gaia and ATLAS light curve covering about 5 years with the epochs of the IRTF and X-shooter spectra overplotted.

In order to compare the amplitudes and durations of the bursts, we fitted a Gaussian to most peaks. Exceptions were the 2010 peak in the CRTS, the 2015 peak in the NEOWISE, and the 2017 peak in the ATLAS c light curves. The 2010 peak in the CRTS light curve is not well defined, while a fit to the other two peaks was attempted, but the results had large uncertainties. The results are summarized in Table 1. Based on the Gaia G and CRTS photometry, the largest amplitude corresponds to the 2023 burst and is ∼1.7 mag, while the smallest amplitude burst was the one in 2017 with an amplitude of ∼1.1 mag. Based on the Gaia G and CRTS data, the 2013 and the 2020 bursts had similar time scales with FWHM of ∼215 days and ∼210 days, respectively, while the 2015 and 2017 bursts had similar, shorter time scales with FWHM of ∼135 days and ∼152 days, respectively. Based on the 2017, 2020, and 2023 bursts, the WISE light curves show slightly lower amplitudes compared to the optical light curves. The $W2$ light curves show ∼30-40% larger amplitudes compared to the $W1$ light curves.

[3] https://exoplanetarchive.ipac.caltech.edu/cgi-bin/Pgram/nph-pgram

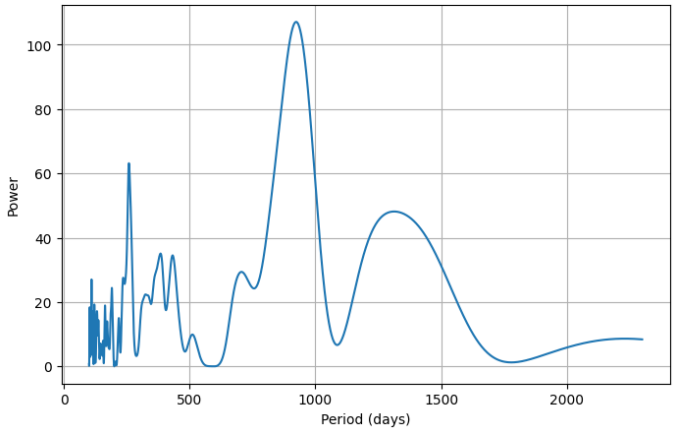

Figure 2. Periodogram based on the CRTS and Gaia G magnitudes.

Table 1. Gaussian fits to bursts.

Year	Band	Amplitude (mag)	Center (MJD−54000)	FWHM (days)
2007	CRTS / Gaia G / ATLAS(o)	1.53 ± 0.07	239 ± 6	168 ± 12
2013	CRTS / Gaia G / ATLAS(o)	1.36 ± 0.04	2441 ± 12	215 ± 11
2015	CRTS / Gaia G / ATLAS(o)	1.55 ± 0.10	3336 ± 6	135 ± 9
2017	CRTS / Gaia G / ATLAS(o)	1.13 ± 0.05	4043 ± 4	152 ± 8
2017	WISE W1	0.63 ± 0.12	3988 ± 47	92 ± 29
2017	WISE W2	0.88 ± 0.15	3998 ± 31	117 ± 26
2020	CRTS / Gaia G / ATLAS(o)	1.51 ± 0.05	5039 ± 4	210 ± 9
2020	ATLAS(c)	2.82 ± 0.07	5069 ± 5	189 ± 6
2020	WISE W1	0.92 ± 0.13	5031 ± 33	217 ± 42
2020	WISE W2	1.20 ± 0.18	5029 ± 35	218 ± 45
2023	ATLAS(c)	2.75 ± 0.06	6180 ± 4	172 ± 5
2023	CRTS / Gaia G / ATLAS(o)	1.66 ± 0.02	6207 ± 2	168 ± 3
2023	WISE W1	0.89 ± 0.04	6127 ± 8	157 ± 9
2023	WISE W2	1.17 ± 0.12	6125 ± 18	171 ± 23

By visual inspection, the optical and infrared light curves seem to be correlated. To quantify this correlation, we interpolated the Gaia G magnitudes at the epochs of the NEOWISE data, and calculated the Pearson correlation coefficients, which are 0.86 between the interpolated Gaia G and $W1$ magnitudes, and 0.88 between the interpolated Gaia G and $W2$ magnitudes. We discuss the positions of the (NEO)WISE data in Appendix A.

Figure 3 shows the $J-H$ versus $H-K$ color-color diagram based on the 2MASS magnitudes, the IRTF photometry, and synthetic photometry based on the X-shooter spectrum, which can be used to estimate the visual extinction. All of the data points are close to the locus of unreddened T Tauri stars, suggesting that Gaia21bja has negligible extinction which does not vary significantly. This result is consistent with the value derived by Luhman & Esplin (2020), and may suggest that the variability is not due to changes in extinction.

3.2. *Spectral energy distribution*

We plotted the Spectral Energy Distribution (SED) of Gaia21bja both in quiescence and during the burst in Figure 4. To construct the SED in quiescence, we used data from Pan-STARRS PS1 (Magnier et al. 2013), 2MASS, and the faintest (NEO)WISE data points from VizieR. As investigated in Appendix A, we consider the (NEO)WISE data points obtained during quiescence as upper limits. For the SED during the burst, we used data from Gaia G and ATLAS during the 2023 burst, JHK magnitudes obtained with the IRTF in 2023, and the brightest (NEO)WISE data

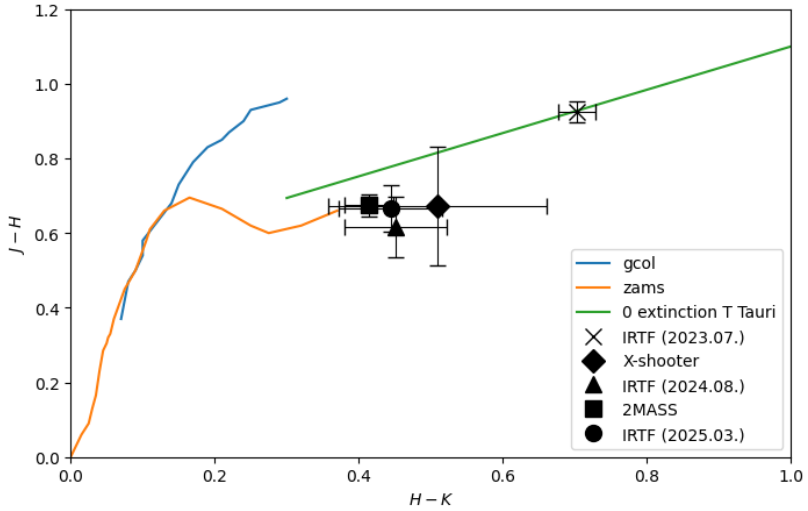

Figure 3. $J - H$ versus $H - K$ color-color diagram. The orange and blue lines correspond to the color of the zero-age main sequence and the giant branch (Bessell & Brett 1988), respectively. The green line shows the locus of unreddened CTTS (Meyer et al. 1997).

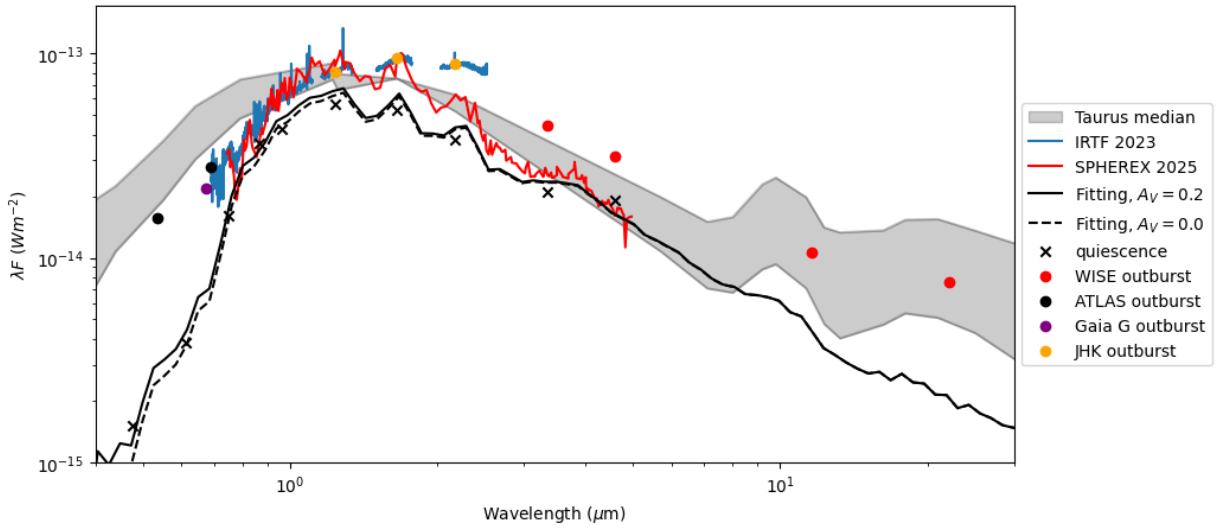

Figure 4. SEDs of Gaia21bja in quiescence (crosses) and during the burst (dots). Spectra from IRTF (blue) and SPHEREx (red) are also overplotted. The 'Taurus median' SED, normalized to the flux at 1.65 μm is overplotted for comparison. The black lines correspond to the best fitting model from Robitaille et al. (2006) corresponding to visual extinctions of 0 mag and 0.2 mag.

points from VizieR. We overplotted the IRTF spectrum obtained during the burst in 2023, and a spectrum obtained by the Spectro-Photometer for the History of the Universe, Epoch of Reionization and Ices Explorer (SPHEREx, Crill et al. 2020, SPHEREx Team 2025) in 2025 July-August. In Figure 4, we overplotted the 'Taurus median', which is based on the SEDs of CTTS in the Taurus region (D'Alessio et al. 1999, Furlan et al. 2006). The shaded area includes the median as well as the lower and upper quartiles, which define the range around the median where 50% of the flux values lie (Furlan et al. 2006).

We calculated the spectral index using the formula by Kuhn et al. (2021) using the [4.5] − [24] color index, as this is the one preferred by the article. We used the photometry from Luhman & Esplin (2020) and obtained $\alpha = -0.51$, which corresponds to Class II (Lada 1987).

In order to characterize the quiescent SED, we used the SED Fitter of Robitaille et al. (2007) and the model grid of Robitaille et al. (2006). This model grid of YSOs is based on the radiation transfer code by (Whitney et al. 2003a,b). The 200,000 SED models cover a large range of stellar masses (from 0.1 to 50 $M_{\odot}$) and evolutionary stages (from embedded protostars to transitional disks). The model consists of a pre-main sequence star surrounded by an accretion disk and a rotationally flattened envelope with bipolar cavities. Scattering and reprocessing of the stellar radiation by dust, as well as the accretion luminosity are taken into account in the model. The SED Fitter fits each of the models to the data, allowing the A_V to be a free parameter, and performs a χ^2 minimization. The best fit model, overplotted in Figure 4 was found to have an A_V of 0.2 mag, however, an A_V of 0 mag provides a similar fit. The best fit effective temperature of 2982 K, found for the model fit, is close to the 3190 ± 75 K derived by Thanathibodee et al. (2022). The very low A_V found in this model fit is consistent with the result from the $J-H$ versus $H-K$ color-color diagram. Assuming an A_V of 0.2 mag has very little effect on the results in Sections 3.4 and 3.5. Furthermore, we investigated, that the mass accretion rate, which is estimated in Sect. 3.5, is most consistent with an A_V of 0 mag. Therefore, for the calculations in the next sections, we assume an A_V of 0 mag.

3.3. *Line detections*

The spectra taken during quiescence with the IRTF/Spex and during burst with the IRTF/Spex and VLT/X-shooter are shown in Figures 5 and 6. In both the X-shooter and IRTF spectrum we discarded values in the wavelength ranges 1.11 μm – 1.16 μm, 1.34 – 1.50 μm, and 1.77 – 2.03 μm, as these are heavily affected by atmospheric effects. We also applied a correction from vacuum to air in the case of the outburst IRTF spectrum using the formula by Morton (2000), as the other two spectra are given in air. For a comparison, we also plotted the X-shooter spectra of EX Lupi during its recent burst (Cruz-Sáenz de Miera et al. 2023) and quiescence (Rigliaco et al. 2020). The IRTF and VLT spectra taken during the burst are similar to those of EXors and CTTS. The CO-bandhead is seen in absorption in quiescence and during the burst. There are various accretion rate tracer lines detected at both epochs during the burst, including the Balmer, Brackett and Paschen series of H I, Ca II, O I, He I, and Na I. However, only a very few and faint accretion tracers are seen in quiescence, suggesting a low mass accretion rate. The line fluxes during the burst and in quiescence are listed in Tables 2 and 3, respectively.

3.4. *Stellar parameters*

We use the quiescence spectra obtained with the IRTF in August 2024 to estimate the effective temperature of the star by comparing it to BT-Settl (AGSS2009) photospheric templates (Allard et al. 2011, Allard et al. 2012, Asplund et al. 2009, Barber et al. 2006). We removed parts of the dataset affected by the telluric correction (as indicated in Section 3.3), as well as data above 1200 nm, as these are affected by the accretion disk. The photospheric templates provide the flux emitted by a star at a given temperature, $\log(g)$, metallicity, and wavelength, which we interpolated whenever needed. We compared the models with $\log(g) = 4$ and [Fe/H] = 0.37 assuming $A_V = 0$ mag to the observed quiescence spectra. We used non-linear least-squares minimization (LMFIT library) in Python for fitting, and the best fitting model corresponds to a temperature of $T = 3000$ K as seen in Figure 7. As we had grid points every 100 K, we estimate the error to be 50 K. This result is also close to the previous SED fitting and the earlier reported value of 3190 ± 75 K (Thanathibodee et al. 2022).

Once the effective temperature and visual extinction are estimated, the stellar luminosity, mass, and radius can be derived following a method previously used by Fiorellino et al. (2021). The stellar luminosity can be derived as

$$L_{\star} = 10^{0.4(M_{\rm bol,\odot} - M_{\rm bol})} L_{\odot} \tag{1}$$

$M_{\rm bol,\odot}$ is the bolometric magnitude of the Sun (Mamajek et al. 2015), and the absolute bolometric magnitude of the star, $M_{\rm bol}$ can be calculated as

$$M_{\rm bol} = (J + BC_J) + 5 - 5\log(d[\rm pc]) \tag{2}$$

where J is the extinction corrected J band magnitude in quiescence (in general, however, for Gaia21bja, no extinction correction was needed) and BC_J is the J band bolometric correction. We used the BC_J estimated for 5-30 Myr stars by Pecaut & Mamajek (2013) for M3 type stars (based on the effective temperature derived above). Based on the above, we calculated $L_{\star} = (4.5 \pm 0.3) \times 10^{-2}\ L_{\odot}$.

To investigate the effect of using an optical band to estimate the stellar luminosity, we used the lowest V-band magnitude found in archival data: $V = 16.4$ mag (Zacharias et al. 2013) and the V-band bolometric correction

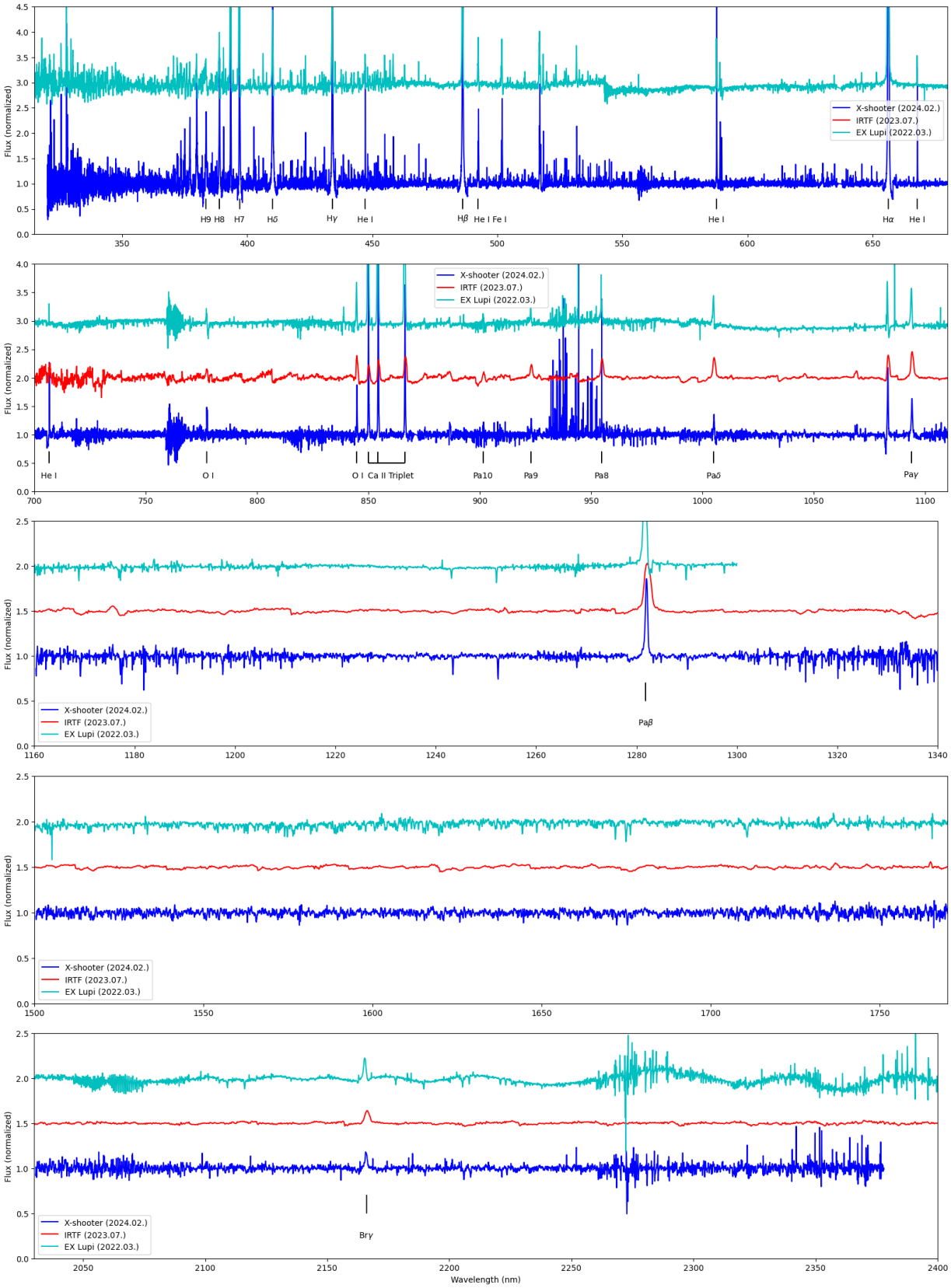

Figure 5. Spectra of Gaia21bja observed during the burst using the IRTF/SpeX and the VLT/X-shooter. We also plotted the outburst spectrum of EX Lupi as a reference.

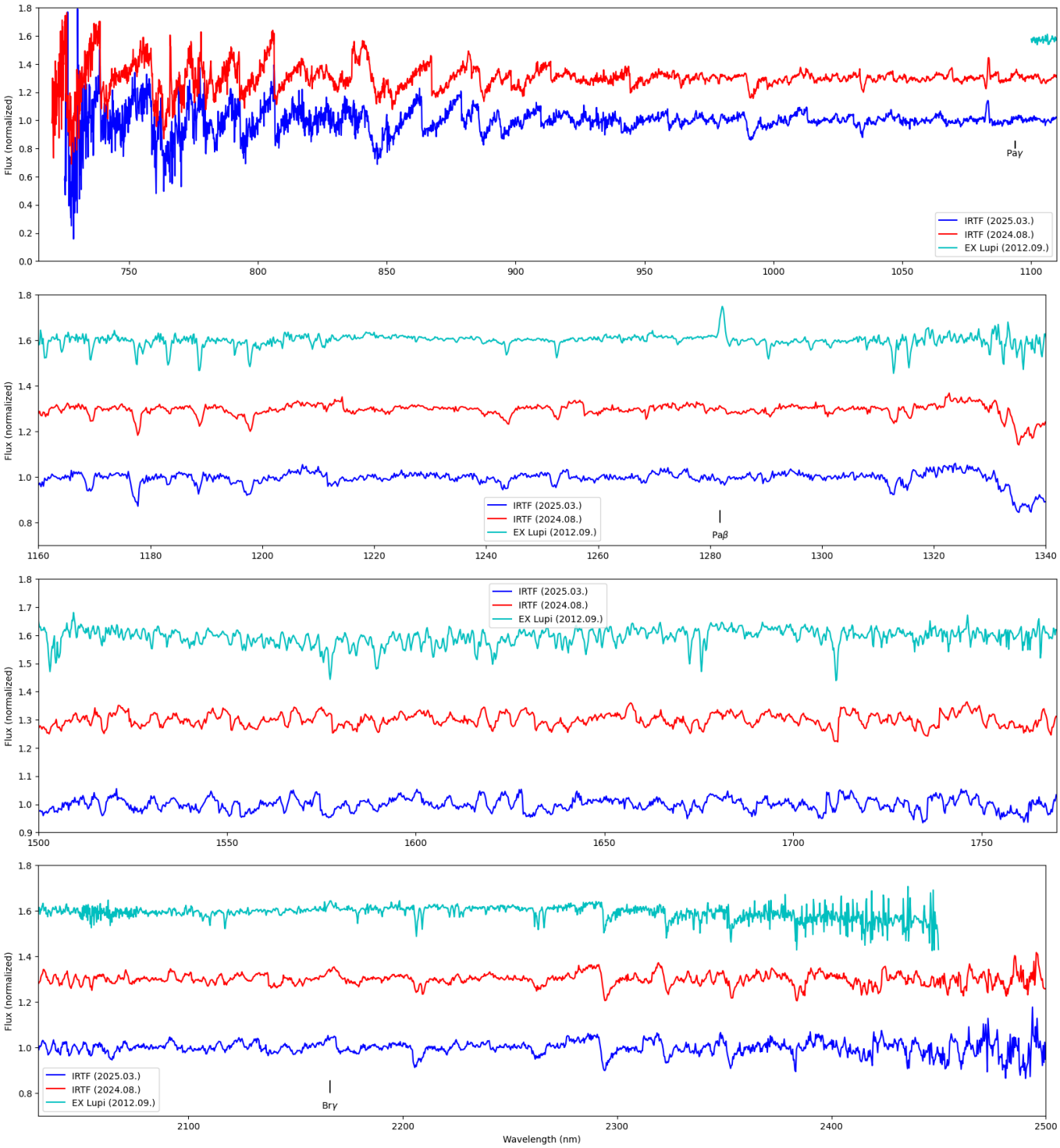

Figure 6. Spectra of Gaia21bja observed during quiescence using IRTF/SpeX. We also plotted the quiescence spectrum of EX Lupi as a reference.

estimated for 5-30 Myr stars by Pecaut & Mamajek (2013). Assuming a 10% error for the V magnitude, we obtained $L_\star = (6.4 \pm 1.3) \times 10^{-2}\ L_\odot$. Since this result is fairly consistent with the one based on the J magnitude, we continue to use the values obtained from the J magnitude in the following.

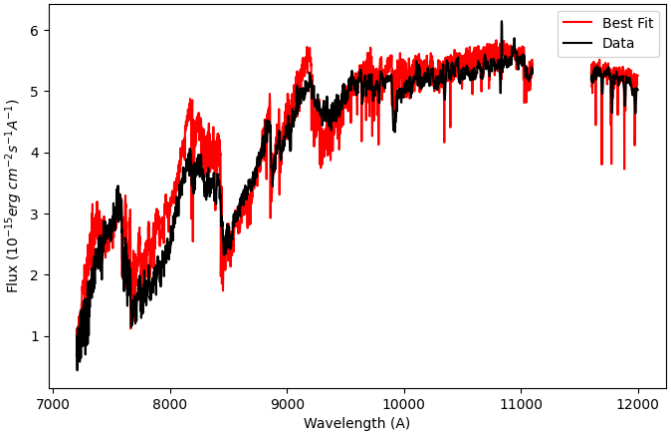

Figure 7. The IRTF spectrum obtained in August 2024 (during quiescence) and the best fitting BT-Settl model, corresponding to a temperature of $T = 3000$ K.

Based on the $L_\star = (4.5 \pm 0.3) \times 10^{-2}\ L_\odot$, the effective temperature derived above, and the evolutionary tracks by Siess et al. (2000), we determined a stellar mass of $M_\star = 0.16 \pm 0.03\ M_\odot$, which corresponds to a metallicity of Z=0.04 and an age of 5.97×10^6 yr. The stellar radius can be derived as

$$R_\star = \frac{1}{2T^2}\sqrt{\frac{L_\star}{\pi\sigma}} \tag{3}$$

where T is the effective temperature and σ is the Stefan-Boltzmann constant. This results in a stellar radius of $R_\star = 0.78 \pm 0.04\ R_\odot$. In the following, we can use the stellar parameters derived in this section to estimate the accretion parameters.

3.5. *Accretion parameters*

The fluxes of the accretion tracer lines listed in Table 2 can be used to estimate the accretion luminosities. Since we found the extinction to be negligible, these fluxes ($f_{\rm line}$) can be directly converted to line luminosities as

$$L_{\rm line} = 4\pi d^2 f_{\rm line} \tag{4}$$

which can be converted to accretion luminosities $L_{\rm acc}$ using the empirical relations from Alcalá et al. (2017). Assuming an inner-disk radius of 5 $R_\star$ (Hartmann et al. 1998), the mass accretion rate can be calculated as

$$\dot{M}_{\rm acc} = 1.25\frac{L_{\rm acc} R_\star}{G M_\star}. \tag{5}$$

where $R_\star$ and $M_\star$ are the radius and mass of the star, respectively.

Since we detected some emission lines in quiescence, we could calculate the mass accretion rate both in quiescence and during the burst. The values during the burst are plotted in Figure 8 and are listed in Table 2. We have discarded lines where the fluxes have more than a 50% error (SNR<2). We did not take into account the He I line at $\lambda = 501.57$ nm, as its flux may trace winds/outflows (Edwards et al. 2006). We also considered visual extinctions above the assumed 0 mag, up to an A_V of 0.5 mag, however, we found the mass accretion rates estimated from the different lines are more consistent with no extinction rather than values of up to an A_V of 0.5 mag, confirming our assumption based on the $J-H$ vs $H-K$ diagram and the SED fitting, that extinction toward Gaia21bja is indeed negligible.

We consider the accretion luminosity and mass accretion rate at each epoch as the variance-weighted average of the values derived from the different lines and their standard deviation as the error. In quiescence, the accretion luminosity and the mass accretion rate were $(3.7 \pm 5.5) \times^{-4} L_\odot$ and $(5.3 \pm 10.7) \times 10^{-11}\ M_\odot\ {\rm yr}^{-1}$ in 2024 August and $(1.7 \pm 0.1) \times 10^{-3} L_\odot$ and $(3.4 \pm 0.7) \times 10^{-10}\ M_\odot\ {\rm yr}^{-1}$ in 2025 March, respectively. During the burst, we obtained an accretion luminosity of $(4.6 \pm 2.6) \times 10^{-3}\ L_\odot$ and a mass accretion rate of $(1.0 \pm 0.5) \times 10^{-9}\ M_\odot\ {\rm yr}^{-1}$ at the epoch of the X-shooter spectrum, and an accretion luminosity of $(6.4 \pm 2.2) \times 10^{-3}\ L_\odot$ and a mass accretion rate of $(1.1 \pm 0.4) \times 10^{-9}\ M_\odot\ {\rm yr}^{-1}$ at the epoch of the IRTF spectrum, suggesting that the accretion luminosity and the

mass accretion rate did not change during the burst. Taking the average of the accretion luminosities derived from the quiescent spectra, $\sim 1.0 \times 10^{-3}$ $L_\odot$, and the average of the accretion luminosities derived during the burst, $\sim 5.5 \times 10^{-3}$ $L_\odot$, the accretion luminosities increased by a factor of ∼5.5 between the quiescent and burst states.

To obtain another estimate of the accretion parameters, we used the SED Fitter of Robitaille et al. (2007), as in Sect. 3.2 for the quiescent SED, and fit also the SED during the burst, in order to obtain bolometric luminosities. The bolometric luminosity given by the model is 9.9×10^{-2} $L_\odot$ during quiescence and 3.3×10^{-1} $L_\odot$ during the burst. Assuming $L_{\rm acc} \sim L_{\rm bol} - L_\star$, the accretion luminosity in quiescence is ~ 0.05 $L_\odot$ and it is ~ 0.29 $L_\odot$ during the burst, assuming the stellar luminosity of 4.5×10^{-2} $L_\odot$ obtained above. Using eqn. 5, the corresponding mass accretion rates are 1.1×10^{-8} $M_\odot$ yr^{-1} during quiescence and 5.7×10^{-8} $M_\odot$ yr^{-1} during the burst, which are more than an order of magnitude above the values obtained using the line luminosities. The difference between the accretion luminosities derived from the SEDs for quiescence and the burst suggests a factor of ∼6 increase between quiescence and the burst, which is similar to what was found for the 2022 burst of EX Lupi (Cruz-Sáenz de Miera et al. 2023). We discuss the accretion parameters in Sect. 4.1.

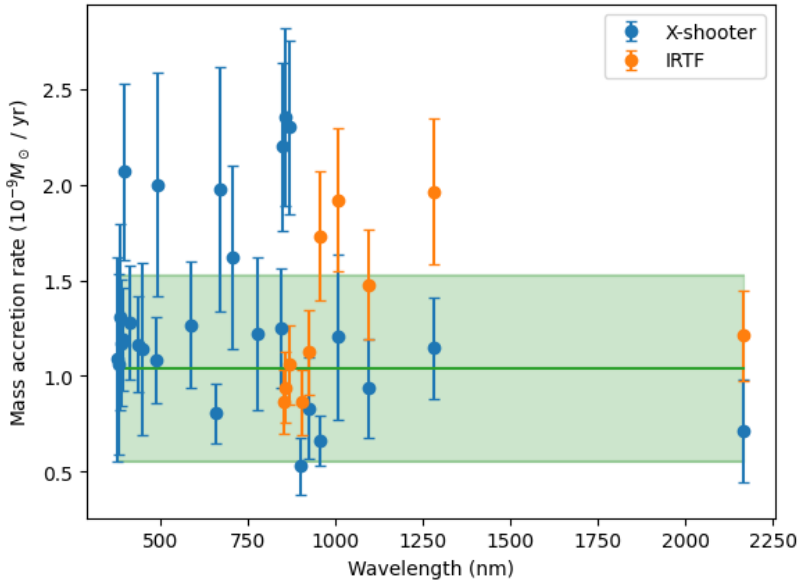

Figure 8. Mass accretion rates during the burst obtained from the line luminosities and the empirical relations of Alcalá et al. (2017). The green line is the average of all the data points weighted by variance. The shaded green area shows the values which are within the standard deviation.

4. DISCUSSION

We analyzed the optical and near-infrared photometry and spectroscopy of the young stellar object Gaia21bja. There are several brightening events with an amplitude up to ∼1.7 mag in Gaia G-band. The duration of these brightening events is about 1.5–2 years. Based on the time scales and amplitudes, the brightenings of Gaia21bja may be consistent with eruptive YSO bursts. In addition to the light curve, its spectra during the burst are similar to those of EXors. Here we discuss the accretion luminosities and mass accretion rates, and the quasi-periodic variability.

4.1. *Accretion parameters*

In Sect. 3.5 we derived accretion parameters using two different methods and found that the accretion parameters increased by a factor of $5.5 - 6$ during the burst. Considering the line luminosities of the detected emission lines and converting them to accretion luminosities using the Alcalá et al. (2017) empirical relations resulted in more than an order of magnitude lower accretion luminosities compared to those obtained from bolometric luminosities derived by SED fitting. The Alcalá et al. (2017) empirical relations assume that the magnetospheric accretion model is applicable, which is the case for CTTS (Hartmann et al. 2016). Magnetospheric accretion is also expected in the case EXor bursts and outbursts (Sicilia-Aguilar et al. 2015). However, recent studies questioned the validity of magnetospheric accretion

for (out)bursts (Cruz-Sáenz de Miera et al. 2023; Fiorellino et al. 2025). In particular, Cruz-Sáenz de Miera et al. (2023) found that accretion luminosities derived for EX Lupi using the empirical relations and those obtained from a slab model may be up to an order of magnitude different. The inconsistency between the results of the two methods used to estimate the accretion luminosities suggests, that similarly to the cases studied by Cruz-Sáenz de Miera et al. (2023) and Fiorellino et al. (2025), the magnetospheric accretion model may not be applicable to the burst of Gaia21bja.

In Figure 9 we compare the accretion luminosities and mass accretion rates to the stellar luminosity and mass, respectively, for Gaia21bja using both methods and compare them to those derived for samples of CTTS and for confirmed eruptive YSOs. For CTTS we used samples towards the Lupus (black symbols, Alcalá et al. 2019), the Chamaeleon I (grey symbols, Manara et al. 2019), and the NGC 1333 (light blue symbols, Fiorellino et al. 2021) regions. The parameters for the EXors and FUors are based on the Outbursting YSOs Catalogue (OYCAT, Contreras Peña et al. 2025) and references therein. The accretion parameters derived from the bolometric luminosity are clearly above the CTTS with similar luminosities and masses. Even the accretion parameters estimated using the empirical relations are among the highest values for similar stellar parameters.

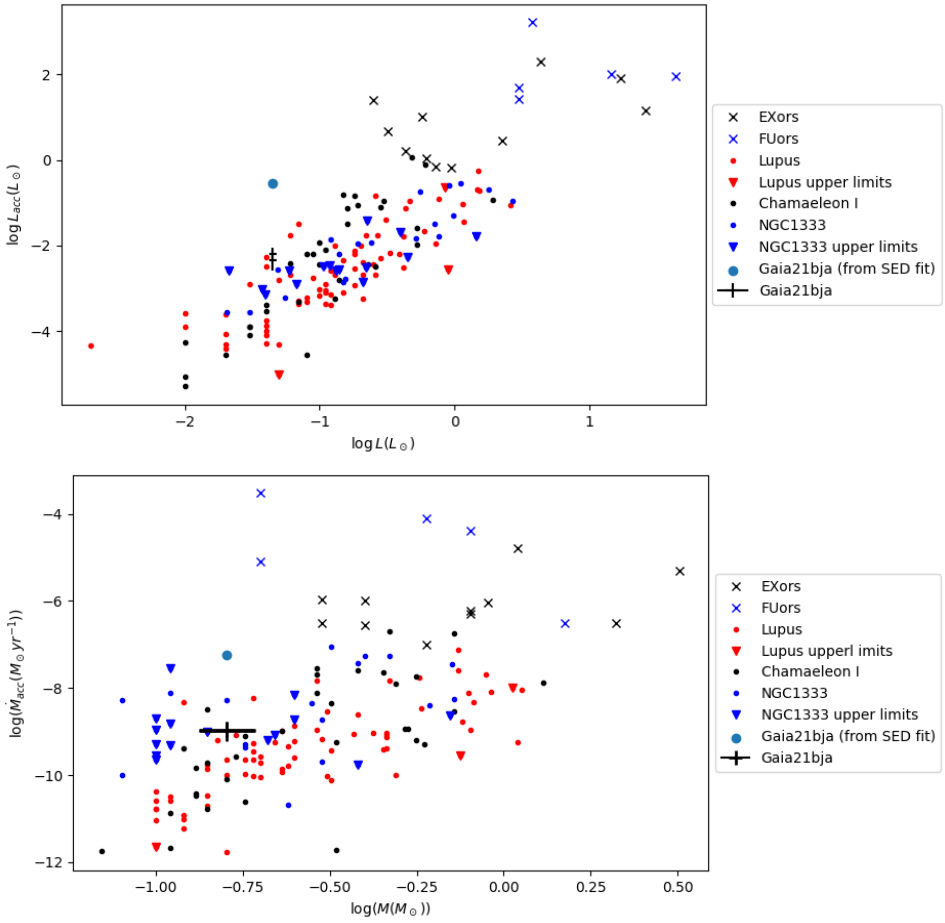

Figure 9. Accretion luminosities ($L_\odot$) versus stellar luminosities ($L_\odot$) (top panel) and mass accretion rates ($M_\odot$ yr^{-1}) versus stellar masses ($M_\odot$) (bottom panel) and their comparison to confirmed EXors and FUors (crosses) and samples of CTTS in the Lupus (red symbols, Alcalá et al. 2019), Chamaeleon I (black symbols, Manara et al. 2019), and NGC 1333 (blue symbols, Fiorellino et al. 2021) regions. The upper limits are marked with downward triangles. The parameters for the EXors and FUors obtained during their outbursts are based on the OYCAT (Contreras Peña et al. 2025) and references therein.

We also compare the derived accretion parameters to those corresponding to the same star-forming region. As a member of Upper Sco, Gaia21bja is most likely an evolved, 5-10 Myr old, pre-main sequence star. This is supported by Fig. 2 of Manara et al. (2020), as the luminosity and effective temperature of Gaia21bja are consistent with the HR diagram of Upper Sco (Gaia21bja is located at $\log T_{\rm eff}(K) = 3.477$, $\log L_\star(L_\odot) = -1.35$). Based on the H$\alpha$ line,

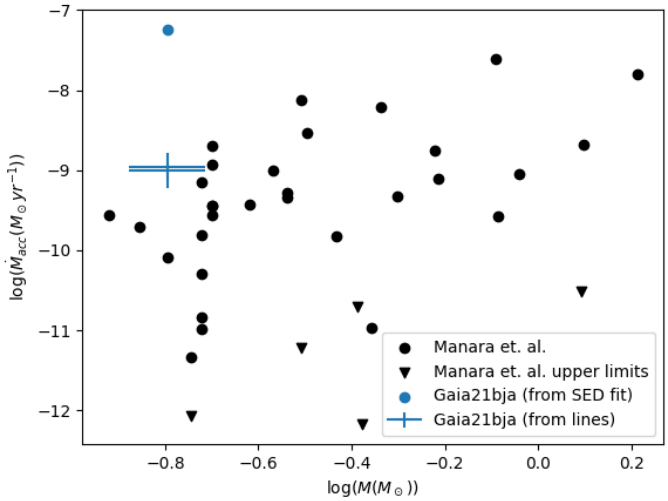

Figure 10. Mass accretion rates versus stellar masses in the Upper Scorpius (Manara et al. 2020).

observed on 2017 July 17, Thanathibodee et al. (2022) selected this star into a list of low accretors. In Figure 10 we plotted the mass accretion rate versus stellar mass of Gaia21bja derived using both methods together with those derived for the members of Upper Sco by Manara et al. (2020) and shown in their Table 1. Figure 10 shows that Gaia21bja is among the lowest mass members of the cluster among those with mass accretion rate estimates. The mass accretion rate of Gaia21bja derived using both methods during its burst is among the highest values for a similar mass in the Upper Sco region. Based on the above comparisons, we suggest that Gaia21bja is an eruptive YSO. Based on its quasi-periodic light curve, Gaia21bja seems to be most consistent with the 'Periodic' group of the OYCAT (Contreras Peña et al. 2025).

4.2. *Quasi-periodic variability*

An interesting characteristics of this star is the quasi-periodic occurrence of the brightening events, which was found for 8 eruptive YSOs so far based on the new catalog by Contreras Peña et al. (2025). The cycle lengths of these brightening events cover a large range from ∼25 days for LRLL54361 (Muzerolle et al. 2013; Le Gouellec et al. 2024) to 1437 days for VVVv32 (Contreras Peña et al. 2017; Guo et al. 2022). The period derived above for Gaia21bja falls in this range: 916 ± 77 days. It was suggested, that these quasi-periodic changes may be due to a stellar or planetary-mass companion interacting with the disk (Hodapp et al. 2012; Yoo et al. 2017; Guo et al. 2022). Assuming this is the case, we can estimate the semi-major axis of the orbit using Kepler's 3rd law

$$\frac{a^3}{T^2} = \frac{GM}{4\pi^2}, \tag{6}$$

where T is the period and M is the total mass. Assuming that the companion's mass m is much smaller than that of the main star (M_*) we get $a = 1.00 \pm 0.08\ AU$. This gives a lower limit for the semi-major axis. However, if m would be comparable to M_*, then the wiggling of the main component would be of the order of a and be detectable by Gaia. Since Gaia has found no signs of a companion, we accept that $m \ll M_*$.

We can also use the fact that Gaia could not detect a component to give an upper limit for the companion's mass. According to Mignard & Klioner (2010), the astrometric accuracy of Gaia is $\theta_{\rm lim} \sim 130\ \mu as$ for sources with Gaia magnitude of 16. Thus, the smallest amount of wiggling Gaia can detect is $\Delta x_{\rm lim} = \theta_{\rm lim} d$, where $\theta_{\rm lim}$ is in radians. The semi-major axis of the main component's orbit is

$$a_* = \frac{m}{M_* + m} a \approx \frac{m}{M_*} a. \tag{7}$$

In the worst case the orbit is oriented such that the minor axis is perpendicular to the line of sight and the main component's wiggle is $\Delta x = 2b_*$, where $b_* = \sqrt{1 - e^2}\ a_*$ is the semi-minor axis of the main component's orbit, where

e is the eccentricity. Putting these together, we get

$$\Delta x_{\rm lim} \geq 2b_*$$
$$\theta_{\rm lim} d \geq 2\sqrt{1-e^2}\frac{m}{M_*}a$$
$$m\sqrt{1-e^2} \leq M_* \frac{\theta_{\rm lim} d}{2a} = 1.6\ M_{\rm Jupiter}$$

where $M_{\rm Jupiter}$ is the mass of Jupiter. Typically $0.1 < \sqrt{1-e^2} < 1$, which is equivalent with an upper limit of around $1-10\ M_{\rm Jupiter}$. This suggests that the component (if exists) is a planetary component.

5. SUMMARY

We studied the photometry and spectroscopy of a Gaia alerted YSO, Gaia21bja. Our main results are summarized below.

- The 20-year-long optical light curve of the star shows at least seven bursts with an amplitude up to 1.7 mag, which appear to be quasi-periodic. Using a Lomb-Scargle periodogram analysis, we derived the most significant period to be 916 ± 77 days.

- Based on a comparison to photospheric templates, we estimated the effective temperature of the star to be $T = 3000 \pm 50$ K. We derived the stellar radius, luminosity, and mass to be $R_\star = 0.78 \pm 0.04\ R_\odot$, $L_\star = (4.5 \pm 0.3) \times 10^{-2}\ L_\odot$, and $M_\star = 0.16 \pm 0.03\ M_\odot$.

- We estimated accretion luminosities and mass accretion rates using two different methods, and found that the accretion parameters of the star increased by a factor of $5.5-6$ during the burst.

Based on the above, we conclude that Gaia21bja is an eruptive YSO, which is most consistent with the 'Periodic' category of the OYCAT (Contreras Peña et al. 2025), the first object in this group which was found from the Gaia Alerts.

We thank the referee for comments and suggestions which helped to improve this paper. We acknowledge the Hungarian National Research, Development and Innovation Office grant OTKA FK 146023. We acknowledge support from the ESA PRODEX contract nr. 4000132054. G. M. and Zs. N. were supported by the János Bolyai Research Scholarship of the Hungarian Academy of Sciences.

F. C. S. M. received financial support from the European Research Council (ERC) under the European Union's Horizon 2020 research and innovation programme (ERC Starting Grant "Chemtrip", grant agreement No 949278).

The IRTF/SpeX data presented here were obtained at the Infrared Telescope Facility, which is operated by the University of Hawaii under contract 80HQTR24DA010 with the National Aeronautics and Space Administration.

This work was also supported by the NKFIH NKKP grant ADVANCED 149943 and the NKFIH excellence grant TKP2021-NKTA-64. Project no. 149943 has been implemented with the support provided by the Ministry of Culture and Innovation of Hungary from the National Research, Development and Innovation Fund, financed under the NKKP ADVANCED funding scheme.

Based on observations made with ESO Telescopes at the La Silla Paranal Observatory under programme ID 0112.C-0201(A) or 112.25XA.001.

This project has received funding from the European Research Council (ERC) via the ERC Synergy Grant ECOGAL (grant 855130). Views and opinions expressed are however those of the author(s) only and do not necessarily reflect those of the European Union or the European Research Council Executive Agency. Neither the European Union nor the granting authority can be held responsible for them.

For this work we have used Python in the Google Colaboratory environment and the libraries NumPy (Harris et al. (2020)), SciPy (Virtanen et al. (2020), Matplotlib (Hunter (2007)), Pandas (pandas development team (2020), McKinney (2010)), LMFIT (Newville et al. (2025), and Astropy (Astropy Collaboration et al. (2013), Astropy Collaboration et al. (2018), Astropy Collaboration et al. (2022)).

We acknowledge ESA *Gaia*, DPAC and the Photometric Science Alerts Team (http://gsaweb.ast.cam.ac.uk/alerts).

Facilities: VLT, IRTF

REFERENCES

Alcalá, J. M., Manara, C. F., France, K., et al. 2019, A&A, 629, A108, doi: 10.1051/0004-6361/201935657

Alcalá, J. M., Manara, C. F., Natta, A., et al. 2017, A&A, 600, A20, doi: 10.1051/0004-6361/201629929

Allard, F., Homeier, D., & Freytag, B. 2011, in Astronomical Society of the Pacific Conference Series, Vol. 448, 16th Cambridge Workshop on Cool Stars, Stellar Systems, and the Sun, ed. C. Johns-Krull, M. K. Browning, & A. A. West, 91, doi: 10.48550/arXiv.1011.5405

Allard, F., Homeier, D., & Freytag, B. 2012, Philosophical Transactions of the Royal Society of London Series A, 370, 2765, doi: 10.1098/rsta.2011.0269

Asplund, M., Grevesse, N., Sauval, A. J., & Scott, P. 2009, ARA&A, 47, 481, doi: 10.1146/annurev.astro.46.060407.145222

Astropy Collaboration, Robitaille, T. P., Tollerud, E. J., et al. 2013, A&A, 558, A33, doi: 10.1051/0004-6361/201322068

Astropy Collaboration, Price-Whelan, A. M., Sipőcz, B. M., et al. 2018, AJ, 156, 123, doi: 10.3847/1538-3881/aabc4f

Astropy Collaboration, Price-Whelan, A. M., Lim, P. L., et al. 2022, ApJ, 935, 167, doi: 10.3847/1538-4357/ac7c74

Audard, M., Ábrahám, P., Dunham, M. M., et al. 2014, in Protostars and Planets VI, ed. H. Beuther, R. S. Klessen, C. P. Dullemond, & T. Henning, 387–410, doi: 10.2458/azu_uapress_9780816531240-ch017

Bailer-Jones, C. A. L., Rybizki, J., Fouesneau, M., Demleitner, M., & Andrae, R. 2021, AJ, 161, 147, doi: 10.3847/1538-3881/abd806

Barber, R. J., Tennyson, J., Harris, G. J., & Tolchenov, R. N. 2006, MNRAS, 368, 1087, doi: 10.1111/j.1365-2966.2006.10184.x

Bessell, M. S., & Brett, J. M. 1988, PASP, 100, 1134, doi: 10.1086/132281

Cody, A. M., & Hillenbrand, L. A. 2018, AJ, 156, 71, doi: 10.3847/1538-3881/aacead

Contreras Peña, C., Lucas, P. W., Kurtev, R., et al. 2017, MNRAS, 465, 3039, doi: 10.1093/mnras/stw2802

Contreras Peña, C., Lee, J.-E., Herczeg, G., et al. 2025, Journal of Korean Astronomical Society, 58, 209, doi: 10.5303/JKAS.2025.58.2.209

Crill, B. P., Werner, M., Akeson, R., et al. 2020, in Society of Photo-Optical Instrumentation Engineers (SPIE) Conference Series, Vol. 11443, Space Telescopes and Instrumentation 2020: Optical, Infrared, and Millimeter Wave, ed. M. Lystrup & M. D. Perrin, 114430I, doi: 10.1117/12.2567224

Cruz-Sáenz de Miera, F., Kóspál, Á., Ábrahám, P., et al. 2022, ApJ, 927, 125, doi: 10.3847/1538-4357/ac477f

Cruz-Sáenz de Miera, F., Kóspál, Á., Abrahám, P., et al. 2023, A&A, 678, A88, doi: 10.1051/0004-6361/202347063

Cushing, M. C., Vacca, W. D., & Rayner, J. T. 2004, PASP, 116, 362, doi: 10.1086/382907

Cutri, R. M., Mainzer, A., Conrow, T., et al. 2015, Explanatory Supplement to the NEOWISE Data Release Products

D'Alessio, P., Calvet, N., Hartmann, L., Lizano, S., & Cantó, J. 1999, ApJ, 527, 893, doi: 10.1086/308103

Drake, A. J., Djorgovski, S. G., Mahabal, A., et al. 2009, ApJ, 696, 870, doi: 10.1088/0004-637X/696/1/870

Edwards, S., Fischer, W., Hillenbrand, L., & Kwan, J. 2006, The Astrophysical Journal, 646, 319, doi: 10.1086/504832

Esplin, T. L., Luhman, K. L., Miller, E. B., & Mamajek, E. E. 2018, The Astronomical Journal, 156, 75, doi: 10.3847/1538-3881/aacce0

Findeisen, K., Hillenbrand, L., Ofek, E., et al. 2013, ApJ, 768, 93, doi: 10.1088/0004-637X/768/1/93

Fiorellino, E., Manara, C. F., Nisini, B., et al. 2021, A&A, 650, A43, doi: 10.1051/0004-6361/202039264

Fiorellino, E., Ábrahám, P., Kóspál, Á., et al. 2024, A&A, 686, A160, doi: 10.1051/0004-6361/202347777

Fiorellino, E., Alcalá, J. M., Manara, C. F., et al. 2025, A&A, 704, A42, doi: 10.1051/0004-6361/202556603

Fischer, W. J., Hillenbrand, L. A., Herczeg, G. J., et al. 2023, in Astronomical Society of the Pacific Conference Series, Vol. 534, Protostars and Planets VII, ed. S. Inutsuka, Y. Aikawa, T. Muto, K. Tomida, & M. Tamura, 355, doi: 10.48550/arXiv.2203.11257

Furlan, E., Hartmann, L., Calvet, N., et al. 2006, ApJS, 165, 568, doi: 10.1086/505468

Ghosh, A., Sharma, S., Ninan, J. P., et al. 2022, ApJ, 926, 68, doi: 10.3847/1538-4357/ac41c2

Giannini, T., Schisano, E., Nisini, B., et al. 2024, ApJ, 967, 41, doi: 10.3847/1538-4357/ad39e2

Giannini, T., Gangi, M., Cruz-Sáenz de Miera, F., et al. 2026, ApJ, 998, 54, doi: 10.3847/1538-4357/ae2be8

Guo, Z., Lucas, P. W., Smith, L. C., et al. 2022, MNRAS, 513, 1015, doi: 10.1093/mnras/stac768
Harris, C. R., Millman, K. J., van der Walt, S. J., et al. 2020, Nature, 585, 357, doi: 10.1038/s41586-020-2649-2
Hartmann, L., Calvet, N., Gullbring, E., & D'Alessio, P. 1998, ApJ, 495, 385, doi: 10.1086/305277
Hartmann, L., Herczeg, G., & Calvet, N. 2016, ARA&A, 54, 135, doi: 10.1146/annurev-astro-081915-023347
Heinze, A. N., Tonry, J. L., Denneau, L., et al. 2018, AJ, 156, 241, doi: 10.3847/1538-3881/aae47f
Herbig, G. H. 1977, ApJ, 217, 693, doi: 10.1086/155615
—. 2008, AJ, 135, 637, doi: 10.1088/0004-6256/135/2/637
Hillenbrand, L. A., Reipurth, B., Connelley, M., Cutri, R. M., & Isaacson, H. 2019, AJ, 158, 240, doi: 10.3847/1538-3881/ab4e16
Hillenbrand, L. A., Contreras Peña, C., Morrell, S., et al. 2018, ApJ, 869, 146, doi: 10.3847/1538-4357/aaf414
Hodapp, K. W., Chini, R., Watermann, R., & Lemke, R. 2012, ApJ, 744, 56, doi: 10.1088/0004-637X/744/1/56
Hodapp, K. W., Denneau, L., Tucker, M., et al. 2020, AJ, 160, 164, doi: 10.3847/1538-3881/abad96
Hodgkin, S. T., Harrison, D. L., Breedt, E., et al. 2021, A&A, 652, A76, doi: 10.1051/0004-6361/202140735
Hunter, J. D. 2007, Computing in Science & Engineering, 9, 90, doi: 10.1109/MCSE.2007.55
Kausch, W., Noll, S., Smette, A., et al. 2015, A&A, 576, A78, doi: 10.1051/0004-6361/201423909
Kenyon, S. J., Hartmann, L. W., Strom, K. M., & Strom, S. E. 1990, AJ, 99, 869, doi: 10.1086/115380
Kuhn, M. A., de Souza, R. S., Krone-Martins, A., et al. 2021, The Astrophysical Journal Supplement Series, 254, 33, doi: 10.3847/1538-4365/abe465
Lada, C. J. 1987, in IAU Symposium, Vol. 115, Star Forming Regions, ed. M. Peimbert & J. Jugaku, 1
Lakeland, B. S., & Naylor, T. 2022, MNRAS, 514, 2736, doi: 10.1093/mnras/stac1477
Lawrence, A., Warren, S. J., Almaini, O., et al. 2007, MNRAS, 379, 1599, doi: 10.1111/j.1365-2966.2007.12040.x
Le Gouellec, V. J. M., Greene, T. P., Hillenbrand, L. A., & Yates, Z. 2024, ApJ, 966, 91, doi: 10.3847/1538-4357/ad2935
Liu, H., Herczeg, G. J., Johnstone, D., et al. 2022, ApJ, 936, 152, doi: 10.3847/1538-4357/ac84d2
Luhman, K. L., & Esplin, T. L. 2020, The Astronomical Journal, 160, 44, doi: 10.3847/1538-3881/ab9599
Luhman, K. L., Herrmann, K. A., Mamajek, E. E., Esplin, T. L., & Pecaut, M. J. 2018, The Astronomical Journal, 156, 76, doi: 10.3847/1538-3881/aacc6d
Magnier, E. A., Schlafly, E., Finkbeiner, D., et al. 2013, ApJS, 205, 20, doi: 10.1088/0067-0049/205/2/20
Mainzer, A., Bauer, J., Grav, T., et al. 2011, ApJ, 731, 53, doi: 10.1088/0004-637X/731/1/53
Mamajek, E. E., Torres, G., Prsa, A., et al. 2015, arXiv e-prints, arXiv:1510.06262. https://arxiv.org/abs/1510.06262
Manara, C. F., Mordasini, C., Testi, L., et al. 2019, A&A, 631, L2, doi: 10.1051/0004-6361/201936488
Manara, C. F., Natta, A., Rosotti, G. P., et al. 2020, A&A, 639, A58, doi: 10.1051/0004-6361/202037949
McKinney, W. 2010, in Proceedings of the 9th Python in Science Conference, ed. Stéfan van der Walt & Jarrod Millman, 56 – 61, doi: 10.25080/Majora-92bf1922-00a
Meyer, M. R., Calvet, N., & Hillenbrand, L. A. 1997, AJ, 114, 288, doi: 10.1086/118474
Mignard, F., & Klioner, S. A. 2010, in IAU Symposium, Vol. 261, Relativity in Fundamental Astronomy: Dynamics, Reference Frames, and Data Analysis, ed. S. A. Klioner, P. K. Seidelmann, & M. H. Soffel, 306–314, doi: 10.1017/S174392130999055X
Modigliani, A., Goldoni, P., Royer, F., et al. 2010, in Society of Photo-Optical Instrumentation Engineers (SPIE) Conference Series, Vol. 7737, Observatory Operations: Strategies, Processes, and Systems III, ed. D. R. Silva, A. B. Peck, & B. T. Soifer, 773728, doi: 10.1117/12.857211
Morton, D. C. 2000, ApJS, 130, 403, doi: 10.1086/317349
Muzerolle, J., Furlan, E., Flaherty, K., Balog, Z., & Gutermuth, R. 2013, Nature, 493, 378, doi: 10.1038/nature11746
Nagy, Z., Ábrahám, P., Kóspál, Á., et al. 2022, MNRAS, 515, 1774, doi: 10.1093/mnras/stac1915
Nagy, Z., Park, S., Ábrahám, P., et al. 2023, MNRAS, 524, 3344, doi: 10.1093/mnras/stad2019
Nagy, Z., Kóspál, Á., Ábrahám, P., et al. 2025, ApJ, 987, 37, doi: 10.3847/1538-4357/add68e
Németh, P. E., Cruz-Sáenz de Miera, F., Kóspál, Á., et al. 2026, A&A, 706, A332, doi: 10.1051/0004-6361/202555332
NEOWISE Team. 2020, NEOWISE-R Single Exposure (L1b) Source Table, IPAC, doi: 10.26131/IRSA144
Newville, M., Otten, R., Nelson, A., et al. 2025, LMFIT: Non-Linear Least-Squares Minimization and Curve-Fitting for Python, 1.3.4, Zenodo, doi: 10.5281/zenodo.16175987
pandas development team, T. 2020, pandas-dev/pandas: Pandas, latest, Zenodo, doi: 10.5281/zenodo.3509134
Park, S., Kóspál, Á., Ábrahám, P., et al. 2022, ApJ, 941, 165, doi: 10.3847/1538-4357/aca01e

Patterson, M. T., Bellm, E. C., Rusholme, B., et al. 2018, Publications of the Astronomical Society of the Pacific, 131, 018001, doi: 10.1088/1538-3873/aae904

Pecaut, M. J., & Mamajek, E. E. 2013, ApJS, 208, 9, doi: 10.1088/0067-0049/208/1/9

Ratzenböck, S., Großschedl, J. E., Möller, T., et al. 2023a, A&A, 677, A59, doi: 10.1051/0004-6361/202243690

Ratzenböck, S., Großschedl, J. E., Alves, J., et al. 2023b, A&A, 678, A71, doi: 10.1051/0004-6361/202346901

Rayner, J. T., Toomey, D. W., Onaka, P. M., et al. 2003, PASP, 115, 362, doi: 10.1086/367745

Rigliaco, E., Gratton, R., Kóspál, Á., et al. 2020, A&A, 641, A33, doi: 10.1051/0004-6361/202038337

Robitaille, T. P., Whitney, B. A., Indebetouw, R., & Wood, K. 2007, ApJS, 169, 328, doi: 10.1086/512039

Robitaille, T. P., Whitney, B. A., Indebetouw, R., Wood, K., & Denzmore, P. 2006, ApJS, 167, 256, doi: 10.1086/508424

Shingles, L., Smith, K. W., Young, D. R., et al. 2021, Transient Name Server AstroNote, 7, 1

Sicilia-Aguilar, A., Fang, M., Roccatagliata, V., et al. 2015, A&A, 580, A82, doi: 10.1051/0004-6361/201525970

Siess, L., Dufour, E., & Forestini, M. 2000, A&A, 358, 593. https://arxiv.org/abs/astro-ph/0003477

Siwak, M., Hillenbrand, L. A., Kóspál, Á., et al. 2023, MNRAS, 524, 5548, doi: 10.1093/mnras/stad2135

Siwak, M., Kóspál, Á., Ábrahám, P., et al. 2025, A&A, 695, A130, doi: 10.1051/0004-6361/202451061

Skrutskie, M. F., Cutri, R. M., Stiening, R., et al. 2003, 2MASS All-Sky Point Source Catalog (PSC), IPAC, doi: 10.26131/IRSA2

Smette, A., Sana, H., Noll, S., et al. 2015, A&A, 576, A77, doi: 10.1051/0004-6361/201423932

Smith, K. W., Smartt, S. J., Young, D. R., et al. 2020, PASP, 132, 085002, doi: 10.1088/1538-3873/ab936e

SPHEREx Team. 2025, SPHEREx Quick Release Spectral Images, IPAC, doi: 10.26131/IRSA629

Szegedi-Elek, E., Ábrahám, P., Wyrzykowski, Ł., et al. 2020, ApJ, 899, 130, doi: 10.3847/1538-4357/aba129

Thanathibodee, T., Calvet, N., Hernández, J., Maucó, K., & Briceño, C. 2022, AJ, 163, 74, doi: 10.3847/1538-3881/ac3ee6

Tonry, J. L., Denneau, L., Heinze, A. N., et al. 2018, PASP, 130, 064505, doi: 10.1088/1538-3873/aabadf

Vacca, W. D., Cushing, M. C., & Rayner, J. T. 2003, PASP, 115, 389, doi: 10.1086/346193

Vernet, J., Dekker, H., D'Odorico, S., et al. 2011, A&A, 536, A105, doi: 10.1051/0004-6361/201117752

Virtanen, P., Gommers, R., Oliphant, T. E., et al. 2020, Nature Methods, 17, 261, doi: 10.1038/s41592-019-0686-2

Whitney, B. A., Wood, K., Bjorkman, J. E., & Cohen, M. 2003a, ApJ, 598, 1079, doi: 10.1086/379068

Whitney, B. A., Wood, K., Bjorkman, J. E., & Wolff, M. J. 2003b, ApJ, 591, 1049, doi: 10.1086/375415

Wright, E. L., Eisenhardt, P. R. M., Mainzer, A. K., et al. 2019, AllWISE Source Catalog, IPAC, doi: 10.26131/IRSA1

—. 2010, AJ, 140, 1868, doi: 10.1088/0004-6256/140/6/1868

Yoo, H., Lee, J.-E., Mairs, S., et al. 2017, ApJ, 849, 69, doi: 10.3847/1538-4357/aa8c0a

Zacharias, N., Finch, C. T., Girard, T. M., et al. 2013, AJ, 145, 44, doi: 10.1088/0004-6256/145/2/44

APPENDIX

A. POSITIONS OF THE (NEO)WISE DATA

Despite the correlation between the optical and (NEO)WISE light curves (Fig. 1), we investigated the positions of the (NEO)WISE data points due to another star (2MASS J16041412-2129089) seen close to Gaia21bja. Figure 11 shows single epoch (NEO)WISE $W1$ and $W2$ light curves as well as the positions of the data points. In the bottom left panel of Figure 11 it is seen that some of the (NEO)WISE data points were obtained toward Gaia21bja (the bottom source in the figure), however, some of the observations were pointed between Gaia21bja and the star seen nearby. As seen in the bottom right panel of Figure 11, which shows the magnitudes versus declinations of the (NEO)WISE data points, in the bright state, the (NEO)WISE source positions are centered on Gaia21bja, while in the faint state, they are between Gaia21bja and 2MASS J16041412-2129089. The reason for this is probably that during the bright state, Gaia21bja is much brighter than 2MASS J16041412-2129089, as indicated by the measured source position close to the nominal position of Gaia21bja. During the faint state, the two sources probably have comparable brightness in the W1 and W2 bands, as indicated by the shift in source position, or the 2MASS source may actually be a bit brighter than Gaia21bja. The lower right panel of Fig. 11, shows how the declinations of the NEOWISE data points change as a function of their brightness. At the brightest state, the data points are centered on Gaia21bja, while in the faintest state, the offset between the data points from Gaia21bja is up to about 3.5″. This is about half of the separation between the two objects, which is about 6.34 arcsec based on the UKIDSS J-band image. Therefore, we consider the *(NEO)WISE* data points obtained during quiescence as upper limits.

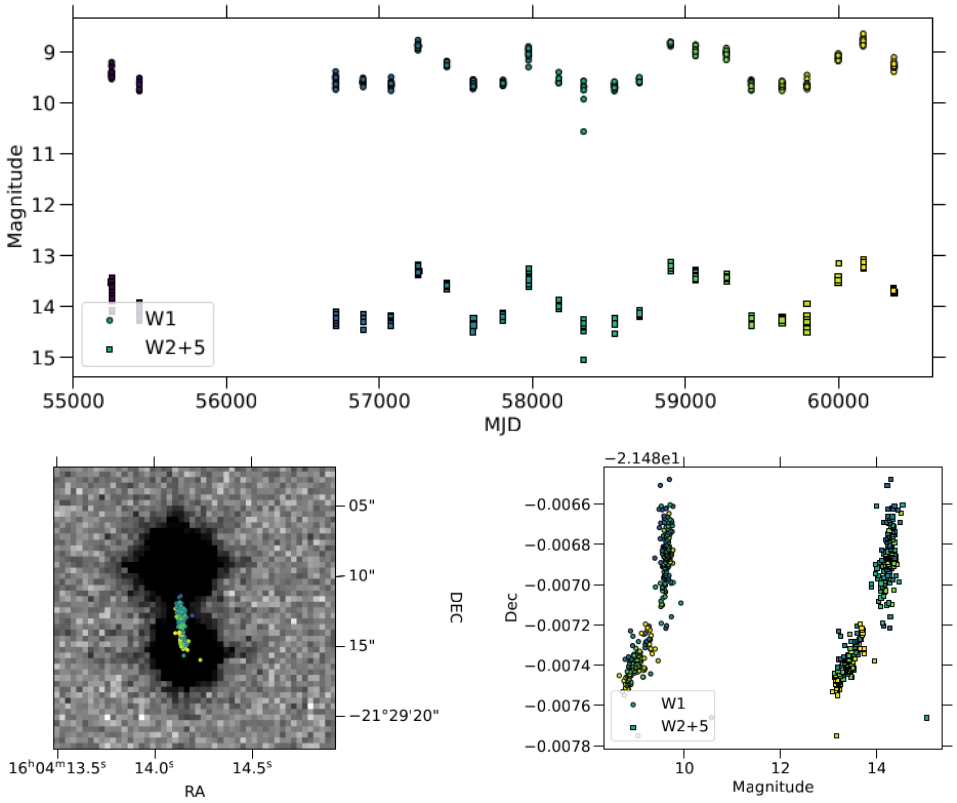

Figure 11. *Top panel:* Single epoch (NEO)WISE $W1$ and $W2$ light curves. *Bottom left panel:* The positions of the (NEO)WISE data points overplotted on a UKIRT Infrared Deep Sky Survey (UKIDSS, Lawrence et al. 2007) J-band image. North is up and east is to the right. Gaia21bja is the southern source. *Bottom right panel:* (NEO)WISE magnitudes versus declination.

B. LINE FLUXES

We present the list of lines which were used to estimate the accretion parameters. Tables 2 and 3 include the line fluxes, accretion luminosities, and mass accretion rates for each accretion tracer obtained during burst and quiescence, respectively. The line fluxes were calculated by numerically integrating the line profiles using Simpson's rule, and the errors were calculated by propagating the error of the individual data points. The lines included in Table 3 have a signal to noise ratio of at least 5.

Table 2. Summary of the line fluxes, accretion luminosities, and mass accretion rates during outburst.

Line	Telescope	$\lambda_{\rm lab}$ (nm)	λ (nm)	F (W/m^2)	$L_{\rm acc}$ ($L_\odot$)	$\dot{M}$ ($M_\odot$/yr)
Hα	X-shooter	656.28	656.20	$(3.35 \pm 0.05) \times 10^{-16}$	$(4.15 \pm 0.09) \times 10^{-3}$	$(8.05 \pm 1.57) \times 10^{-10}$
Hβ	X-shooter	486.13	486.06	$(8.40 \pm 0.53) \times 10^{-17}$	$(5.58 \pm 0.40) \times 10^{-3}$	$(1.08 \pm 0.22) \times 10^{-9}$
Hγ	X-shooter	434.05	433.96	$(5.61 \pm 0.49) \times 10^{-17}$	$(6.01 \pm 0.58) \times 10^{-3}$	$(1.17 \pm 0.25) \times 10^{-9}$
Hδ	X-shooter	410.17	410.10	$(4.65 \pm 0.54) \times 10^{-17}$	$(6.59 \pm 0.82) \times 10^{-3}$	$(1.28 \pm 0.30) \times 10^{-9}$
H7	X-shooter	397.01	396.80	$(5.96 \pm 0.61) \times 10^{-17}$	$(1.07 \pm 0.12) \times 10^{-2}$	$(2.07 \pm 0.46) \times 10^{-9}$
H8	X-shooter	388.90	388.84	$(3.20 \pm 0.60) \times 10^{-17}$	$(6.05 \pm 1.21) \times 10^{-3}$	$(1.17 \pm 0.33) \times 10^{-9}$
H9	X-shooter	383.54	383.48	$(2.58 \pm 0.79) \times 10^{-17}$	$(6.74 \pm 2.16) \times 10^{-3}$	$(1.31 \pm 0.49) \times 10^{-9}$
H10	X-shooter	379.79	379.74	$(1.89 \pm 0.72) \times 10^{-17}$	$(5.47 \pm 2.17) \times 10^{-3}$	$(1.06 \pm 0.47) \times 10^{-9}$
H11	X-shooter	377.06	377.04	$(1.58 \pm 0.68) \times 10^{-17}$	$(5.60 \pm 2.53) \times 10^{-3}$	$(1.09 \pm 0.54) \times 10^{-9}$
Paβ	X-shooter	1281.81	1281.66	$(2.93 \pm 0.35) \times 10^{-17}$	$(5.91 \pm 0.74) \times 10^{-3}$	$(1.15 \pm 0.27) \times 10^{-9}$
Paγ	X-shooter	1093.81	1093.68	$(2.61 \pm 0.41) \times 10^{-17}$	$(4.81 \pm 0.95) \times 10^{-3}$	$(9.34 \pm 2.58) \times 10^{-10}$
Paδ	X-shooter	1004.94	1004.82	$(1.99 \pm 0.49) \times 10^{-17}$	$(6.21 \pm 1.87) \times 10^{-3}$	$(1.21 \pm 0.43) \times 10^{-9}$
Pa8	X-shooter	954.60	954.42	$(9.60 \pm 0.35) \times 10^{-18}$	$(3.40 \pm 0.14) \times 10^{-3}$	$(6.61 \pm 1.31) \times 10^{-10}$
Pa9	X-shooter	922.90	922.78	$(1.05 \pm 0.23) \times 10^{-17}$	$(4.28 \pm 1.09) \times 10^{-3}$	$(8.31 \pm 2.65) \times 10^{-10}$
Pa10	X-shooter	901.49	901.32	$(6.49 \pm 1.17) \times 10^{-18}$	$(2.72 \pm 0.56) \times 10^{-3}$	$(5.28 \pm 1.50) \times 10^{-10}$
Brγ	X-shooter	2166.12	2165.11	$(5.61 \pm 1.53) \times 10^{-18}$	$(3.68 \pm 1.19) \times 10^{-3}$	$(7.13 \pm 2.70) \times 10^{-10}$
He I	X-shooter	447.15	447.10	$(5.60 \pm 1.81) \times 10^{-18}$	$(5.89 \pm 2.02) \times 10^{-3}$	$(1.14 \pm 0.45) \times 10^{-9}$
He I + Fe I	X-shooter	492.19	492.34	$(8.91 \pm 1.99) \times 10^{-18}$	$(1.03 \pm 0.22) \times 10^{-2}$	$(2.00 \pm 0.58) \times 10^{-9}$
He I	X-shooter	587.56	587.50	$(1.21 \pm 0.18) \times 10^{-17}$	$(6.53 \pm 1.14) \times 10^{-3}$	$(1.27 \pm 0.33) \times 10^{-9}$
He I	X-shooter	667.82	667.74	$(6.60 \pm 1.36) \times 10^{-18}$	$(1.02 \pm 0.26) \times 10^{-2}$	$(1.98 \pm 0.64) \times 10^{-9}$
He I	X-shooter	706.52	706.44	$(4.20 \pm 0.79) \times 10^{-18}$	$(8.34 \pm 1.85) \times 10^{-3}$	$(1.62 \pm 0.48) \times 10^{-9}$
Ca II (K)	X-shooter	393.37	393.34	$(3.97 \pm 0.46) \times 10^{-17}$	$(6.14 \pm 0.74) \times 10^{-3}$	$(1.19 \pm 0.27) \times 10^{-9}$
Ca II	X-shooter	849.80	849.70	$(3.82 \pm 0.17) \times 10^{-17}$	$(1.13 \pm 0.05) \times 10^{-2}$	$(2.20 \pm 0.44) \times 10^{-9}$
Ca II	X-shooter	854.21	854.12	$(4.93 \pm 0.19) \times 10^{-17}$	$(1.21 \pm 0.05) \times 10^{-2}$	$(2.35 \pm 0.47) \times 10^{-9}$
Ca II	X-shooter	866.21	866.12	$(4.25 \pm 0.19) \times 10^{-17}$	$(1.19 \pm 0.05) \times 10^{-2}$	$(2.30 \pm 0.46) \times 10^{-9}$
O I	X-shooter	777.31	777.10	$(5.89 \pm 1.22) \times 10^{-18}$	$(6.29 \pm 1.66) \times 10^{-3}$	$(1.22 \pm 0.40) \times 10^{-9}$
O I	X-shooter	844.64	844.54	$(8.71 \pm 1.27) \times 10^{-18}$	$(6.43 \pm 1.01) \times 10^{-3}$	$(1.25 \pm 0.31) \times 10^{-9}$
Paβ	IRTF	1281.81	1282.11	$(4.87 \pm 0.03) \times 10^{-17}$	$(1.01 \pm 0.01) \times 10^{-2}$	$(1.96 \pm 0.38) \times 10^{-9}$
Brγ	IRTF	2166.12	2166.51	$(8.75 \pm 0.20) \times 10^{-18}$	$(6.24 \pm 0.18) \times 10^{-3}$	$(1.21 \pm 0.24) \times 10^{-9}$
Ca II	IRTF	849.80	850.06	$(1.48 \pm 0.03) \times 10^{-17}$	$(4.45 \pm 0.11) \times 10^{-3}$	$(8.63 \pm 1.69) \times 10^{-10}$
Ca II	IRTF	854.21	854.54	$(1.91 \pm 0.03) \times 10^{-17}$	$(4.85 \pm 0.08) \times 10^{-3}$	$(9.41 \pm 1.84) \times 10^{-10}$
Ca II	IRTF	866.21	866.59	$(1.85 \pm 0.03) \times 10^{-17}$	$(5.46 \pm 0.10) \times 10^{-3}$	$(1.06 \pm 0.21) \times 10^{-9}$
Paγ	IRTF	1093.81	1094.14	$(3.78 \pm 0.03) \times 10^{-17}$	$(7.62 \pm 0.12) \times 10^{-3}$	$(1.48 \pm 0.29) \times 10^{-9}$
Paδ	IRTF	1004.94	1005.13	$(2.91 \pm 0.03) \times 10^{-17}$	$(9.90 \pm 0.15) \times 10^{-3}$	$(1.92 \pm 0.37) \times 10^{-9}$
Pa8	IRTF	954.60	954.79	$(2.32 \pm 0.04) \times 10^{-17}$	$(8.93 \pm 0.17) \times 10^{-3}$	$(1.73 \pm 0.34) \times 10^{-9}$
Pa9	IRTF	922.90	923.09	$(1.36 \pm 0.03) \times 10^{-17}$	$(5.79 \pm 0.18) \times 10^{-3}$	$(1.12 \pm 0.22) \times 10^{-9}$
Pa10	IRTF	901.49	901.72	$(9.94 \pm 0.29) \times 10^{-18}$	$(4.45 \pm 0.16) \times 10^{-3}$	$(8.63 \pm 1.71) \times 10^{-10}$

Table 3. Summary of the line fluxes, accretion luminosities, and mass accretion rates during quiescence.

Line	Telescope	$\lambda_{\rm lab}$ (nm)	λ (nm)	F (W/m^2)	$L_{\rm acc}$ ($L_\odot$)	$\dot{M}$ ($M_\odot$/yr)
Brγ	IRTF (2025.03.)	2166.12	2165.11	$(2.97 \pm 0.19) \times 10^{-18}$	$(1.73 \pm 0.13) \times 10^{-3}$	$(3.35 \pm 0.70) \times 10^{-10}$
Paβ	IRTF (2024.08.)	1281.81	1281.69	$(3.45 \pm 0.28) \times 10^{-18}$	$(6.11 \pm 0.52) \times 10^{-4}$	$(1.19 \pm 0.25) \times 10^{-10}$
Brγ	IRTF (2024.08.)	2166.12	2167.97	$(2.32 \pm 0.13) \times 10^{-18}$	$(1.29 \pm 0.08) \times 10^{-3}$	$(2.50 \pm 0.51) \times 10^{-10}$
Paγ	IRTF (2024.08.)	1093.81	1094.33	$(1.96 \pm 0.23) \times 10^{-18}$	$(1.94 \pm 0.28) \times 10^{-4}$	$(3.77 \pm 0.92) \times 10^{-11}$